

# Pulse shape simulation for the reduced charge collection layer in $p$ -type high-purity germanium detectors

P. Zhang<sup>1</sup>, W. Dai<sup>1</sup>, Q. Zhang<sup>1</sup>, F. Hagemann<sup>2</sup>, O. Schulz<sup>2</sup>, C. Alvarez-Garcia<sup>2</sup>,  
L. Yang<sup>1</sup>, Q. Yue<sup>1</sup>, Z. Zeng<sup>1</sup>, J. Cheng<sup>1,3</sup>, H. Ma<sup>1,a</sup>

<sup>1</sup> Department of Engineering Physics, Tsinghua University, Beijing 100084, China

<sup>2</sup> Max-Planck-Institut für Physik, Garching, München 85748, Germany

<sup>3</sup> School of Physics and Astronomy, Beijing Normal University, Beijing 100875, China

Received: date / Accepted: date

**Abstract**  $P$ -type high-purity germanium (HPGe) detectors are widely used across many scientific domains, and current data analysis methods have served well in many use cases. However, applications like low-background experiments that search for rare physics, such as dark matter, neutrinoless double-beta decay, and coherent elastic neutrino-nucleus scattering, could profit a lot from a more detailed understanding of the detector response close to the surface. The outer  $n^+$  electrode of the  $p$ -type HPGe detector forms a layer with reduced charge collection, and events originating here can be a critical background source in such experiments. If the difference in detector pulse shape between detector surface and bulk events is known, it can be used to identify and veto these background events. However, a faithful simulation of the detector response in this surface region is difficult and has not been available as a standard method so far. We present a novel three-dimensional pulse shape simulation method for this reduced charge collection (RCC) layer. We have implemented this method as a new feature in the open-source simulation package *SolidStateDetectors.jl* and show a validation of the numerical simulation results with analytical calculations. An experimental study using a  $p$ -type HPGe detector also validates our approach. The current implementation supports  $p$ -type HPGe detectors of fairly arbitrary geometry, but is easily adaptable to  $n$ -type detectors by adjusting the impurity density profile of the layer. It should also be adaptable to other semiconductor materials in a straightforward fashion.

## 1 Introduction

$P$ -type high-purity germanium (HPGe) detectors have been a mainstay in nuclear and particle physics for decades due to their excellent energy resolution. Applications that require a detailed understanding of the detector signal response still

face challenges though: experiments like rare event searches can take advantage of the intrinsically low background of HPGe. However, the intrinsic background of the detector and especially the surrounding parts is still not low enough for ultralow-background experiments such as direct dark matter detections [1–4], neutrinoless double-beta decay searches [5–7], and coherent elastic neutrino-nucleus scattering detections [8–11]. Such experiments use detailed analysis of the detector signal shapes to distinguish signal from background events to further lower their effective background, but this is not an easy task.

The inhomogeneous electrical and weighting fields of large-volume HPGe detectors, together with the distinct drift behavior between bulk and surface regions, are both a blessing and a curse for such use cases: they result in different signal shapes for different event topologies that are associated with signal and background. However, they also make faithful simulation of such detectors a hard problem. Because of this, experiments have often relied on a data-driven approach to build digital pulse shape processing (DSP) procedures and statistical and machine-learning models for background discrimination [12–18]. This data-driven approach has been successful, but is also limited, as the underlying truth of the data sets that the models are built on is not known event by event. Simulation-based and data-verified models would be the gold standard and have the potential for higher discriminatory power with better control of systematic effects.

Modern detector simulation packages like *SolidStateDetectors.jl* (*SSD.jl*) [19, 20] can calculate detector fields and simulate charge drift in the detector bulk and can also be used to infer critical values like impurity profile parameters from measurements [21]. A detailed simulation of HPGe near-surface effects on the charge drift, however, has not been easily available.

For  $p$ -type HPGe detectors in low-background experiments, the surface plays a special role. The surface  $n^+$  elec-

<sup>a</sup>e-mail: mahao@tsinghua.edu.cn (corresponding author)

trode of a  $p$ -type HPGe detector is typically fabricated through thermal diffusion of lithium, resulting in a heavily doped region with a thickness of  $\sim 0.5\text{--}1$  mm. However, this process introduces a layer in the  $n^+$  electrode that is almost inactive close to the surface, with its charge collection efficiency increasing as a function of depth: due to the weak electric field in this region and a higher trapping (or recombination) rate [22], charge carriers are prone to sudden termination, leading to incomplete charge collection. Thus, charge depositions in this layer are either not registered at all or exhibit a measured energy lower than their true energy. It is sometimes called dead layer, inactive layer, or transition layer in the literature. For clarity, we will call it the reduced charge collection (RCC) layer in this paper. These RCC layer events constitute a significant background component in rare-event searches [12, 23–26].

As the bulk material of the detector crystal is very radiopure, a large part of the background typically originates outside of the detector and on its surface. Background sources that emit alpha, beta, or low-energy gamma particles then deposit most of their energy in the detector close to the surface. As the layer has reduced charge collection, the energy of these events can be shifted into the signal region. Thus, it is important to distinguish them from actual signal events based on the shape of the signal pulse.

We want to study the charge drift of RCC layer events and develop a pulse shape simulation method that can both deepen our understanding of the underlying detector physics and enable a more precise evaluation of the signal efficiencies of pulse shape discrimination techniques [5, 6]. Realistic simulations can also generate clean datasets with known ground truth for developing advanced discrimination techniques [12].

We chose the open-source modular software package *SolidStateDetectors.jl* [19] as the technical basis for our RCC layer charge drift implementation. *SSD.jl* is actively developed and maintained, has a modular and therefore extensible design, and already supports first-principle charge trapping and diffusion handling. It provided us with a solid basis to add mechanistic, non-heuristic RCC layer simulation. The code used to run the simulations in this paper is now freely available as of version 0.11.0 of *SSD.jl*.

## 2 Method

Figure 1 illustrates the basic structure of the  $n^+$  electrode of a  $p$ -type HPGe detector. Because of the thermal diffusion of lithium, the donor concentration decreases rapidly from the surface inward, reaching equilibrium with the acceptor concentration at the  $p$ - $n$  boundary. When a reverse bias voltage is applied, the detector is further depleted. The depletion region extends outward from the  $p$ - $n$  boundary in both directions, with the macroscopic electric field oriented toward the  $p$ -type

region. Consequently, the detector can be divided into three distinct regions from the surface inward:

1)  $n$ -type non-depleted neutral region: this region is characterized by an extremely high concentration of donor impurities ( $\sim 10^{14}\text{--}10^{17}\text{ cm}^{-3}$ ), very short charge carrier lifetimes ( $O(\mu\text{s})$ ), and no electric field [22]. In this region, the donor impurities are ionized [27, 28], but this region remains electrically neutral overall.

2)  $n$ -type depleted region: here, charge carriers exhibit long lifetimes ( $O(\text{ms})$ ) [28]. The donor impurities are ionized and the carriers are depleted. The boundary between the  $n$ -type depleted region and the  $n$ -type neutral region is termed the full-depletion boundary, where the electric field is exactly zero, see Figure 1. The electric field strength in this region increases with the distance to the full-depletion boundary. Following the convention of our previous research, the depth from the detector surface to this boundary is termed the full depletion depth (FDD) [22].

3)  $p$ -type depleted region: this region features a strong electric field and long charge carrier lifetimes ( $O(\text{ms})$ ) [28].

With "sensitive region", we refer to the detector bulk volume with full charge collection efficiency (CCE). RCC layer refers to the outside, including the whole  $n$ -type neutral region and a small part of the  $n$ -type depleted region, as shown in Figure 1. Following the convention of our previous research [22], the depth from the detector surface to the boundary between the sensitive region and the RCC layer is termed the full charge collection depth (FCCD), which is also conventionally regarded as the depth of the RCC layer.

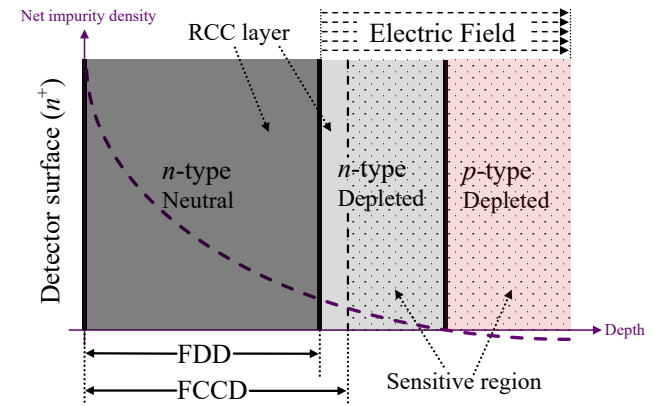


**Fig. 1** Schematic structure of the  $n^+$  electrode of a  $p$ -type HPGe detector. From the surface inward, there are  $n$ -type neutral region (dark gray),  $n$ -type depleted region (light gray), and  $p$ -type depleted region (pink). The net impurity density profile, illustrated as a purple dashed line, crosses zero at the  $p$ - $n$  boundary. The region with non-zero electric field is marked with parallel dashed lines. The sensitive region (full charge collection) is marked with dotted area, and the left near-surface region is the RCC layer. FDD and FCCD are also marked.

The motion of charge carriers involves four physical processes [20, 22, 29]:

- 1) Drift under the electric field: carriers undergo directional drift, which only occurs in the depleted region with non-zero electric field.
- 2) Diffusion: random thermal motion of the carriers.
- 3) Self-repulsion: mutual repulsion between carriers causes charge clouds to expand. This results in a correlation between total energy deposition and charge cloud size, which in turn can result in an energy dependence of the pulse shape.
- 4) Trapping (or recombination): carrier drift may terminate suddenly due to the trapping effect.

## 2.1 Ionized impurity density profile

Ionized impurities refer to impurities with ionized atoms regardless of whether the carriers are depleted, including donors (doped) and acceptors (already existing in *p*-type Ge crystal). To model the physical processes in the RCC layer, we first need to establish the ionized impurity density profiles. For acceptor impurities, we assume a constant density [22]. For donor impurities, which are introduced through thermal diffusion at the  $n^+$  electrode, this work follows the calculations described in Reference [22]. Therefore, the net ionized impurity density profile throughout the crystal is described by

$$N_{I,\text{net}}(x) = N_d(x) - N_a, \quad (1)$$

$$N_d(x) = N_s \cdot \operatorname{erfc}\left(\frac{x}{2\sqrt{D_{\text{Li}}t_{\text{an}}}}\right), \quad (2)$$

$$\log_{10}(N_s/\text{cm}^{-3}) = 21.27 - \left(\frac{2610 \text{ K}}{T_{\text{an}}}\right), \quad (3)$$

$$D_{\text{Li}} = D_0 \cdot \exp\left(-\frac{H}{RT_{\text{an}}}\right), \quad (4)$$

where  $x$  is the depth from the  $n^+$  surface,  $N_{I,\text{net}}$  is the net ionized impurity profile,  $N_d$  is the donor impurity profile,  $N_a$  is the constant acceptor impurity density,  $N_s$  is the saturated surface lithium concentration,  $D_{\text{Li}}$  is the diffusivity of lithium in germanium,  $t_{\text{an}}$  is the annealing time,  $T_{\text{an}}$  is the annealing temperature,  $R$  is the gas constant (1.98 cal/K),  $D_0$  is the diffusivity constant, and  $H$  is the activation energy. For  $T_{\text{an}} \in [473 \text{ K}, 873 \text{ K}]$ ,  $D_0 = 2.5 \times 10^{-3} \text{ cm}^2/\text{s}$ ,  $H = 11800 \text{ cal}$ . For  $T_{\text{an}} \in [873 \text{ K}, 1273 \text{ K}]$ ,  $D_0 = 1.3 \times 10^{-3} \text{ cm}^2/\text{s}$ ,  $H = 10700 \text{ cal}$  [22].

Figure 2 shows the impurity density profiles in the RCC layer under typical parameter choices, with the depth of the *p-n* boundary (where the net ionized impurity density equals zero) marked by a purple dashed line.

## 2.2 Charge-carrier mobilities

We consider three dominant factors that affect the mobilities of carriers (electrons and holes)  $\mu_{e/h}$  in our approach: ion-

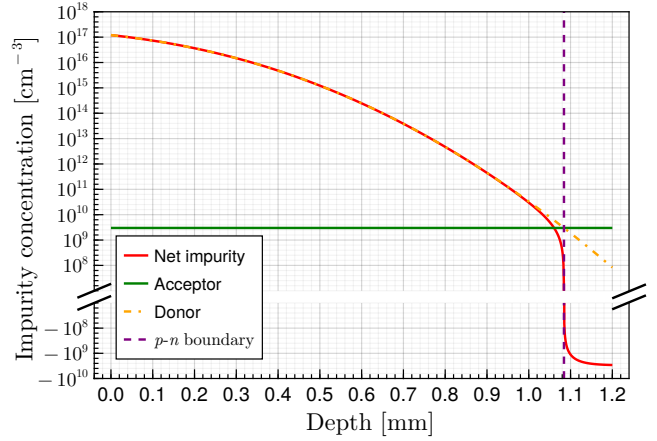


**Fig. 2** Donor (orange dashed), acceptor (green), and net (red) ionized impurity density profiles in the RCC layer with  $N_a = 3 \times 10^9 \text{ cm}^{-3}$ ,  $T_{\text{an}} = 623 \text{ K}$ ,  $t_{\text{an}} = 18 \text{ min}$ , and the saturated surface lithium concentration. The *p-n* boundary is marked with a purple dashed line.

ized impurity scattering ( $\mu_{e/h,I}$ ), neutral impurity scattering ( $\mu_{e/h,N}$ ), and acoustic phonon scattering ( $\mu_{e/h,A}$ ) [30, 31]. Neutral impurities refer to unionized atoms, such as carbon, oxygen, silicon, etc., which may originate from germanium crystal purification and growth processes [30, 32, 33]. They are assumed to be uniformly distributed in the crystal. The electrons/holes mobilities  $\mu_e/\mu_h$  are calculated using Equations (5)–(8) and Equations (9)–(12), respectively [22, 30, 31]:

$$\frac{1}{\mu_e} = \frac{1}{\mu_{e,I}} + \frac{1}{\mu_{e,N}} + \frac{1}{\mu_{e,A}}, \quad (5)$$

$$\mu_{e,I} = \frac{2.44 \times 10^{18} \cdot T^{1.5}/N_I}{\ln(2.50 \times 10^{14} \cdot T^2/N_I)}, \quad (6)$$

$$\mu_{e,N} = \frac{3.00 \times 10^{19}}{N_N} \cdot (T^{0.5} + 1.93 \cdot T^{-0.5}), \quad (7)$$

$$\mu_{e,A} = 9.32 \times 10^7 \cdot T^{-1.5}, \quad (8)$$

$$\frac{1}{\mu_h} = \frac{1}{\mu_{h,I}} + \frac{1}{\mu_{h,N}} + \frac{1}{\mu_{h,A}}, \quad (9)$$

$$\mu_{h,I} = \frac{2.35 \times 10^{17} \cdot T^{1.5}/N_I}{\ln(9.13 \times 10^{13} \cdot T^2/N_I)} + \frac{1.51 \times 10^{18} \cdot T^{1.5}/N_I}{\ln(5.8 \times 10^{14} \cdot T^2/N_I)}, \quad (10)$$

$$\mu_{h,N} = \frac{4.46 \times 10^{29}}{N_N} \cdot (T^{0.5} + 4.28 \cdot T^{-0.5}), \quad (11)$$

$$\mu_{h,A} = 7.77 \times 10^7 \cdot T^{-1.5}, \quad (12)$$

where  $\mu_e$ ,  $\mu_{e,I}$ ,  $\mu_{e,N}$ ,  $\mu_{e,A}$ ,  $\mu_h$ ,  $\mu_{h,I}$ ,  $\mu_{h,N}$ , and  $\mu_{h,A}$  have units of  $\text{cm}^2 \cdot \text{V}^{-1} \cdot \text{s}^{-1}$ ,  $N_I$  ( $= N_a + N_d$ ) is the ionized impurity density [ $\text{cm}^{-3}$ ],  $N_N$  is the neutral impurity density [ $\text{cm}^{-3}$ ], and  $T$  is the crystal temperature [K].

Concentration of neutral impurities is determined by matching the calculated sensitive-region hole mobility (using above equations) to the experimentally measured value [22, 30, 31]. Under typical parameters (sensitive-region hole mobility adopts the IEEE standard —  $42000 \text{ cm}^2 \cdot \text{V}^{-1} \cdot \text{s}^{-1}$  and  $T = 90 \text{ K}$ ), the neutral impurity density is determined to be  $5.677 \times 10^{15} \text{ cm}^{-3}$ . Figure 3 presents the mobility curves for holes and electrons with above parameter choices. When getting closer to the  $n^+$  surface, the heavily doped lithium impurities significantly reduce the carrier mobility.

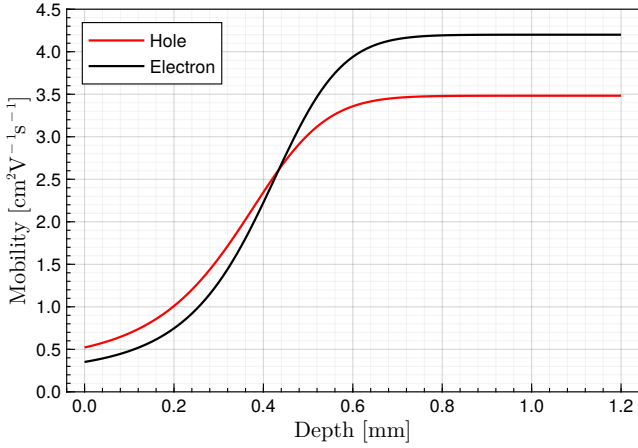


**Fig. 3** Mobilities of electrons (black) and holes (red) in the RCC layer when adopting the IEEE standard value of hole mobility in the sensitive region ( $42000 \text{ cm}^2 \cdot \text{V}^{-1} \cdot \text{s}^{-1}$ ) and  $T = 90 \text{ K}$ .

### 2.3 Charge-carrier diffusion, self-repulsion, and trapping

The charge carrier diffusion process is simulated as a random walk with a step length depending on the diffusion coefficients [20]. The diffusion coefficients  $D_{e/h}$  are calculated from the mobilities  $\mu_{e/h}$  using the Einstein relation [20, 22, 29]:

$$D_{e/h} = \frac{k_B T}{e} \cdot \mu_{e/h}, \quad (13)$$

where  $k_B$  is the Boltzmann constant and  $e$  is the elementary charge.

The carrier self-repulsion effect is simulated by computing the electric field contribution of other carriers and superimposing them onto the static electric field at each drift step for each carrier [20]. The total electric field experienced by the  $k$ -th carrier at time  $t$  is given by

$$\hat{E}_k(\hat{r}_k(t)) = \hat{E}(\hat{r}_k(t)) + \sum_{j \neq k} \frac{q_j}{4\pi\epsilon(\hat{r}_k) |\hat{r}_k - \hat{r}_j|^2} \frac{\hat{r}_k - \hat{r}_j}{|\hat{r}_k - \hat{r}_j|}, \quad (14)$$

where  $\hat{r}_k(t)$  represents the position of the  $k$ -th carrier at time  $t$ ,  $\hat{E}(\hat{r}_k(t))$  denotes the static electric field at that position,  $q_j$  is the charge of the  $j$ -th carrier, and  $\epsilon(\hat{r}_k)$  is the permittivity.

We employ a constant-lifetime trapping model [22, 30, 31, 34], but assume different lifetimes in the sensitive region and the RCC layer. Therefore, our trapping model has four parameters: electron/hole lifetimes in the RCC layer  $\tau_{e/h,R}$ , and in the sensitive region  $\tau_{e/h,S}$ , respectively. For this paper, we set  $\tau_{e/h,S}$  to 1 ms [28], a typical value for high-purity germanium. However, in the RCC layer, the extremely high donor impurity density makes carriers more prone to trapping, resulting in significantly shorter lifetimes than those in the sensitive region. The lifetimes  $\tau_{e/h,R}$  must be determined by experimental calibration. According to the Shockley-Ramo theorem [35], the induced signal  $Q_{e/h}(t)$  is given by

$$Q_{e/h}(t) = Q_{e/h,A}(t) + Q_{e/h,R}(t) + Q_{e/h,S}(t), \quad (15)$$

$$Q_{e/h,A}(t) = w(\hat{r}_{e/h}(t)) q_{e/h}(t), \quad (16)$$

$$Q_{e/h,TR}(t) = \sum_{i \in R(t)} w(\hat{r}_{e/h}(t_i)) q_{e/h}(t_i) \frac{dt_i}{\tau_{e/h,R}}, \quad (17)$$

$$Q_{e/h,TS}(t) = \sum_{i \in S(t)} w(\hat{r}_{e/h}(t_i)) q_{e/h}(t_i) \frac{dt_i}{\tau_{e/h,S}}, \quad (18)$$

$$q_{e/h}(t) = q_{e/h}(0) - q_{e/h,R}(t) - q_{e/h,TS}(t), \quad (19)$$

$$q_{e/h,TR}(t) = \sum_{i \in R(t)} q_{e/h}(t_{i-1}) \frac{dt_i}{\tau_{e/h,R}}, \quad (20)$$

$$q_{e/h,TS}(t) = \sum_{i \in S(t)} q_{e/h}(t_{i-1}) \frac{dt_i}{\tau_{e/h,S}}, \quad (21)$$

where  $dt_i$  is the time step length for the  $i$ -th step of drift,  $Q_{e/h,A}(t)$  denotes the induced signal contributed by alive carriers at time  $t$ ,  $Q_{e/h,TR}(t)$  denotes the induced signal contributed by carriers trapped in the RCC layer,  $Q_{e/h,TS}(t)$  denotes the induced signal contributed by carriers trapped in the sensitive region,  $q_{e/h}(t)$  denote the charges of alive carriers,  $q_{e/h,TR}(t)$  denote the charges of carriers trapped in the RCC layer,  $q_{e/h,TS}(t)$  denote the charges of carriers trapped in the sensitive region,  $\hat{r}_{e/h}(t)$  are the carrier drift paths,  $w(\hat{r}_{e/h}(t))$  are the weighting potentials,  $R(t)/S(t)$  denote the parts of the drift path in the RCC layer and the sensitive region, respectively.

### 2.4 Charge collection efficiency

Based on the aforementioned physical models, we can simulate both the paths of carriers and the induced signals of RCC layer events. Furthermore, we can calculate the CCE curve

of the RCC layer  $f_{\text{CCE}}$  and its uncertainty [22, 36] with

$$f_{\text{CCE}}(x) = \frac{A_p(x)}{Ne}, \quad (22)$$

$$\frac{\sigma_f}{f} = \frac{1}{\sqrt{N}} = \frac{1}{\sqrt{E/E_0}}, \quad (23)$$

where  $x$  is the depth of the simulated single-site event from the detector surface,  $A_p$  is the amplitude of the simulated charge pulse,  $N$  is the initial number of the simulated charge carrier pairs, and  $E_0$  is the ionization energy for germanium.

The CCE curve has been proven to be crucial for interpreting experimental spectra and correcting distortions in the raw simulated energy spectra in the low-energy region because alpha, beta, and low-energy gamma particles from outside have a higher probability to deposit energy close to the surface [22, 36]. For each event, we denote the simulated deposited energies and depths with  $(E_i, x_i)$ . The raw simulated total energy  $E_{\text{raw}}$ , the total energy corrected with CCE curve  $E_{\text{w/}}$ , and total energy corrected without CCE curve  $E_{\text{w/o}}$  are given by

$$E_{\text{raw}} = \sum_i E_i, \quad (24)$$

$$E_{\text{w/}} = \sum_i f_{\text{CCE}}(x_i) E_i, \quad (25)$$

$$E_{\text{w/o}} = \sum_i \Theta(x_i - \text{FCCD}) E_i, \quad (26)$$

where  $\Theta(x - \text{FCCD})$  is the step function with discontinuity at  $x = \text{FCCD}$ . The  $f_{\text{CCE}}(x)$  and  $\Theta(x - \text{FCCD})$  are illustrated in Figure 4.

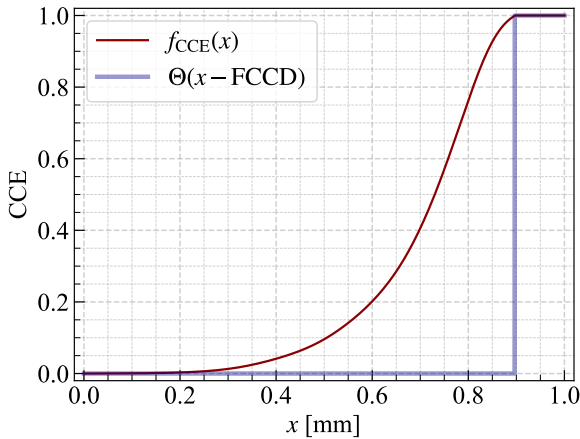


**Fig. 4** Illustration of the CCE curve  $f_{\text{CCE}}(x)$  and the step function  $\Theta(x - \text{FCCD})$  with  $\text{FCCD} = 0.9$  mm.

For  $p$ -type HPGe detectors, in most cases, electrons in the RCC layer contribute negligibly to the induced signal on the  $p^+$  contact because the weighting potential there is nearly zero [25, 29, 37]. Thus, the CCE approximately equals the

fraction of holes that escape the RCC layer before getting trapped or recombined, reach the sensitive region, and get collected by the  $p^+$  electrode. One can determine the FCCD through pulse shape simulation but also experimentally, by matching the experimentally measured energy spectrum with the energy spectrum simulated using a Monte-Carlo software like Geant4 [36, 38–41].

### 3 Method validation

We validate our simulation method by comparing the simulated CCE curve with a theory-based analytical calculation [22].

In the theory-based approach, we compute the CCE in the RCC layer by solving the one-dimensional hole transport equation analytically. For this, we consider three holes-transport physics processes: drift under the electric field, diffusion, and trapping.

In the numerical simulation, we disable the self-repulsion process and the signal contribution from electrons here, for direct comparison with the analytical results.

#### 3.1 Test geometry

We perform our validation on a hypothetical true-coaxial HPGe detector with a 1 mm inner radius, 10 mm outer radius, and 10 mm height, with the coordinate origin set at the center of the bottom surface of the detector, see Figure 5. While not a common detector geometry in practice, the high symmetry enables an analytical solution of the problem.

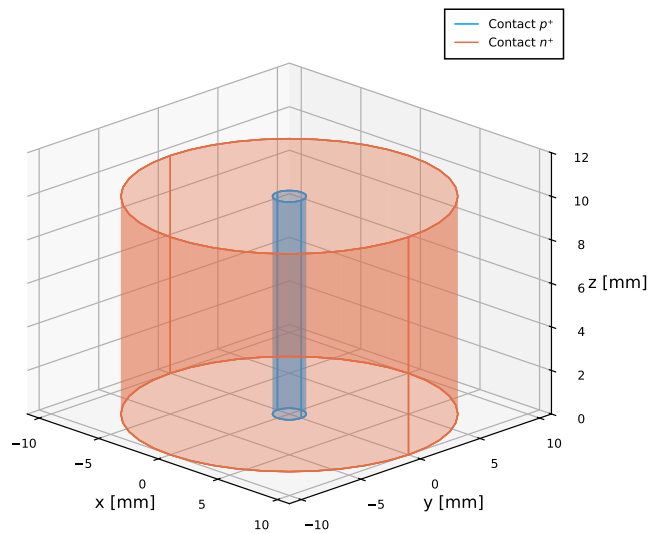


**Fig. 5** Visualization of the simulated hypothetical true-coaxial HPGe detector geometry for the analytical validation.



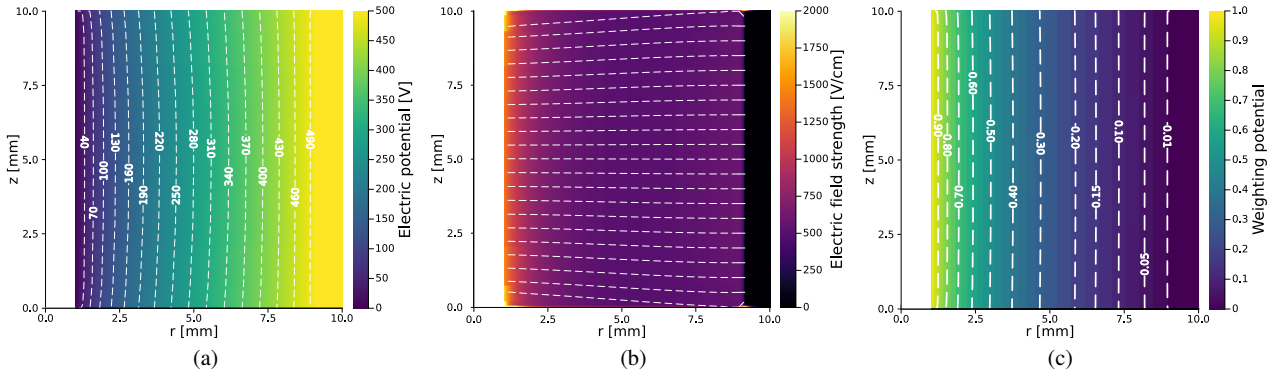


**Fig. 6** The electric potential (dashed lines are the equipotential contours) (a), the electric field (white lines are the electric field lines) (b), and the weighting potential of the  $p^+$  contact (dashed lines are the equipotential contours) (c) of the true-coaxial HPGe detector, as calculated with *SSD.jl*

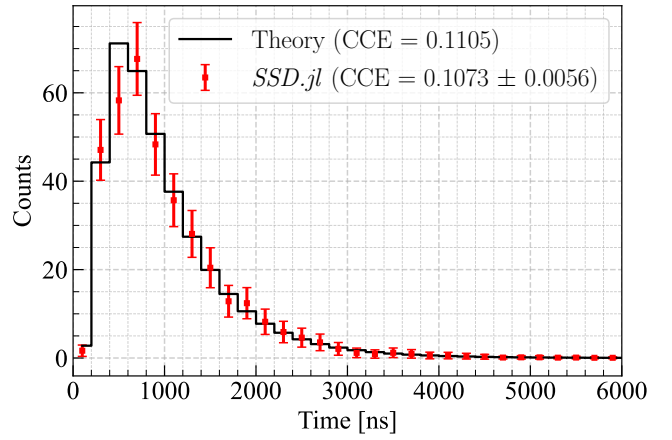
The  $n^+$  electrode of the detector is modeled with lithium impurity doping via thermal diffusion. We assume that the surface lithium concentration is at its saturation level, the annealing time  $t_{\text{an}}$  is 18 minutes, the annealing temperature  $T_{\text{an}}$  is 623 K, the acceptor impurity density is  $1 \times 10^{10} \text{ cm}^{-3}$ , and the bias voltage is 500 V. These parameters result in an  $n$ -type region with a depth of  $\sim 1 \text{ mm}$ . Figure 6 shows the electric potential, weighting potential, and electric field, as calculated with *SSD.jl*. The center point in the  $z$  direction ( $z = 5 \text{ mm}$ ) exhibits sufficient uniformity in the  $z$  direction, which allows us to use the one-dimensional analytical method to calculate the CCE curve of the RCC layer and compare it with the simulated CCE curve.

### 3.2 Charge collection efficiency validation

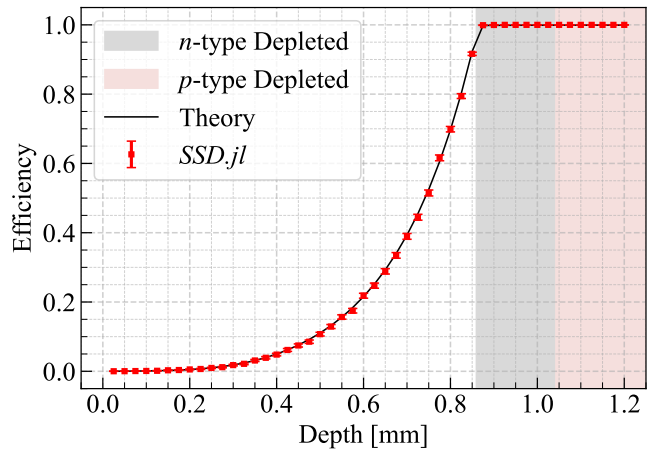
We use both the numerical simulation and the analytical approach to compute the drift of hole clouds generated by events that all have a deposited energy of 10 keV (corresponding to 3389 holes). All holes in the charge cloud of a single event start from the same position simultaneously for both two approaches.

Figure 7 shows the distribution of the time when the holes arrive at the  $p$ - $n$  boundary for a starting depth of 0.5 mm from the surface. The integral of this curve divided by the initial hole number (3389) is the charge collection efficiency of the event, see Equation 22. We observe that the analytical results lie within  $1 \sigma$  of the simulations (using the estimated Poisson fluctuation).

In addition to the arrival time, we compare the depth dependency of the CCE by generating events at different depths in the RCC layer. Figure 8 shows that the two CCE curves are also in very good agreement between numerical simulation and analytical solution.



**Fig. 7** Analytically calculated (black) and numerically simulated (red) distributions of the arrival times of holes at the  $p$ - $n$  boundary. The holes originate from a single-site event with an energy of 10 keV deposited at a depth of 0.5 mm from the surface. The time bin width is set at 200 ns to achieve adequate counting statistics for the simulated results, although the analytical results were calculated with a bin width of 1 ns.



**Fig. 8** Analytically calculated (black) and numerically simulated (red) CCE curves of the RCC layer, calculated by generating events at different depths with an energy of 10 keV.

### 3.3 Pulse shape validation

The numerical simulation generates pulse shapes directly. We can also generate semi-analytical pulse shapes by convolving the analytically derived distribution of hole arrival time at the  $p$ - $n$  boundary with a numerically simulated pulse of a single hole originating exactly at the  $p$ - $n$  boundary, as demonstrated in Figure 9. Figure 10 compares the numerical and semi-analytical pulse shapes for events generated at various depths in the RCC layer. Again, we see very good consistency between the simulation and analytical approaches.

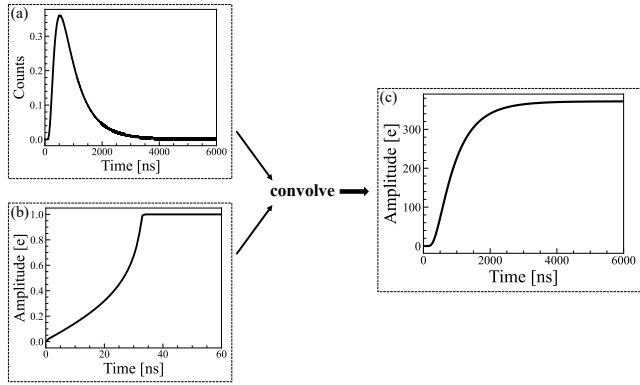


**Fig. 9** Illustration of the pulse shape calculation via the analytical method. (a) Distribution of hole arrival time at the  $p$ - $n$  boundary (the time bin width is 1 ns). (b) The pulse shape of a single hole originating from the  $p$ - $n$  boundary. (c) The pulse shape of the event originating from the RCC layer.

## 4 Results and discussions

### 4.1 Experimental setup and detector fields

We conducted a measurement on a  $p$ -type Broad Energy Germanium detector (BEGe) with an uncollimated  $^{133}\text{Ba}$  source centered at the top of the detector, see Figure 11. The  $n^+$  electrode of the detector was heavily doped with lithium impurities via thermal diffusion. The detector parameters are listed in Table 1 [22, 29]. Figure 11 shows the  $r$ - $z$  cross-section of the crystal. It also shows the surface sampling points that we use in the following as starting points for several charge-drift simulations. The sampling positions include points from the bottom, bottom corner, side, top corner, and top, which are used to display the results along the surface in several plots below. The figure also shows the center-to-surface angle  $\theta$  that we define as

$$\theta = \arctan\left(\frac{z_s - H_c/2}{r_s}\right) \quad (27)$$

with radial and vertical coordinates  $r_s$  and  $z_s$  of the surface point, and the crystal height  $H_c$  ( $= 42.6$  mm).

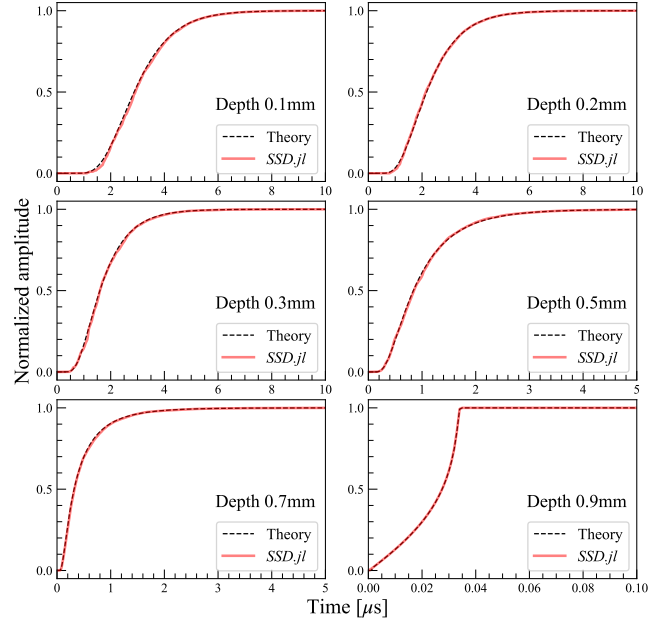


**Fig. 10** Analytically calculated (black) and numerically simulated (red) pulse shapes of events originate at different depths (0.1, 0.2, 0.3, 0.5, 0.7, 0.9 mm) in the RCC layer. Note the shorter time ranges for larger depths (closer to the sensitive region).

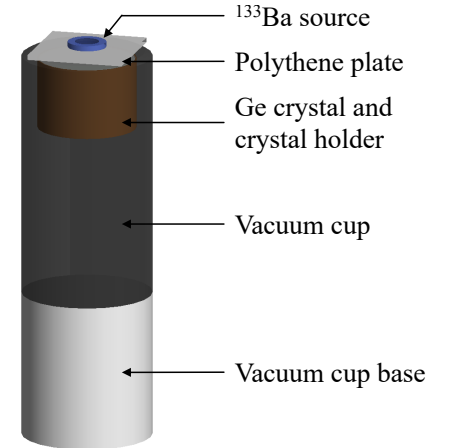


**Fig. 11** Experimental setup. The  $^{133}\text{Ba}$  source was centered at the top of the detector. A polythene plate was placed between the source and the detector to reduce pile-up events.

The electric potential, the electric field, and the weighting potential of the BEGe detector are again calculated using *SSD.jl*, see Figure 13. In the region near the  $p^+$  contact, the electric field, the weighting potential, and the gradient of the weighting potential are much larger than in the rest of the detector volume.

### 4.2 Drift paths and pulse shapes

Figure 14 illustrates the simulated charge carrier drift paths in the sensitive region and in the RCC layer. In the sensitive

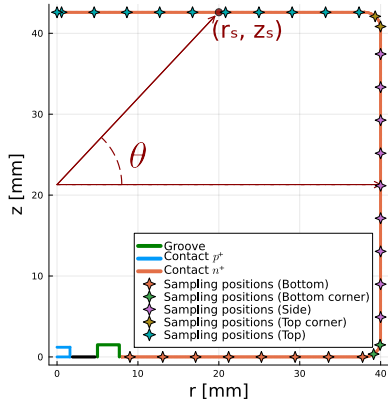


**Fig. 12** The  $r$ - $z$  cross-section of the detector crystal. Also shown are the surface sampling positions (from the bottom, bottom corner, side, top corner, and top) that we use as charge cloud starting points in several following plots, and our definition of the center-to-surface angle  $\theta$ , see Equation 27.

**Table 1** Parameters of the BEGe detector (hole and electron lifetimes are assumed to be identical in this work).

Parameters	Values	Source
Crystal radius	40 mm	Manufacturer
Crystal height	42.6 mm	Manufacturer
$p^+$ electrode hole radius	1.6 mm	Manufacturer
$p^+$ electrode hole height	1.2 mm	Manufacturer
Corner radius	2 mm	Manufacturer
Groove inner radius	5 mm	Typical value
Groove depth	1.5 mm	Typical value
Groove outer radius	8 mm	Typical value
Crystal temperature	90 K	Typical value
Bias voltage	4500 V	Experiment
Surface $n^+$ annealing temperature	623 K	Experiment
Surface $n^+$ annealing time	18 min	Experiment
Surface $n^+$ lithium density	$1.2 \times 10^{17} \text{ cm}^{-3}$	Typical value
Acceptor impurity density	$0.3 \times 10^{10} \text{ cm}^{-3}$	Experiment
Sensitive region hole lifetime	1 ms	Typical value
Sensitive region electron lifetime	1 ms	Typical value
RCC layer hole lifetime	800 ns	Experiment
RCC layer electron lifetime	800 ns	Experiment

region, carriers approximately drift along the electric field lines before getting collected or drifting into the RCC layer. In contrast, in the RCC layer, carriers initially undergo a very slow random diffusion. An electron will keep diffusing until reaching the  $n^+$  contact or getting trapped. Even if it steps into the depleted region, it will "bounce back" due to the electric field there. However, for a hole, once it steps into the depleted region, it will drift rapidly along the electric field lines until it is collected on the  $p^+$  contact, inducing a significant signal.

Figures 15 and 16 depict the normalized simulated pulse shapes of events originating at the  $p$ - $n$  boundary (located

in the sensitive region) and at a depth of 0.5 mm from the surface (located in the RCC layer), respectively, at the sampling positions annotated in Figure 12. Electronic response and electrical noise are not simulated. These pulse shapes are divided into five batches with regard to where the event originates: the bottom, bottom corner, side, top corner, and top.

In most areas (far away from the  $p^+$  contact), the pulse shapes from the  $p$ - $n$  boundary first undergo a slow rise, followed by a rapid rise. This rapid rise is caused by holes drifting into the high-weighting-potential-gradient and high-electric-field region, which is near the  $p^+$  contact in this case, see Figure 13. The moment of the rapid rise depends on the hit position of the event. Generally, the rise will occur earlier when the position is closer to the  $p^+$  contact.

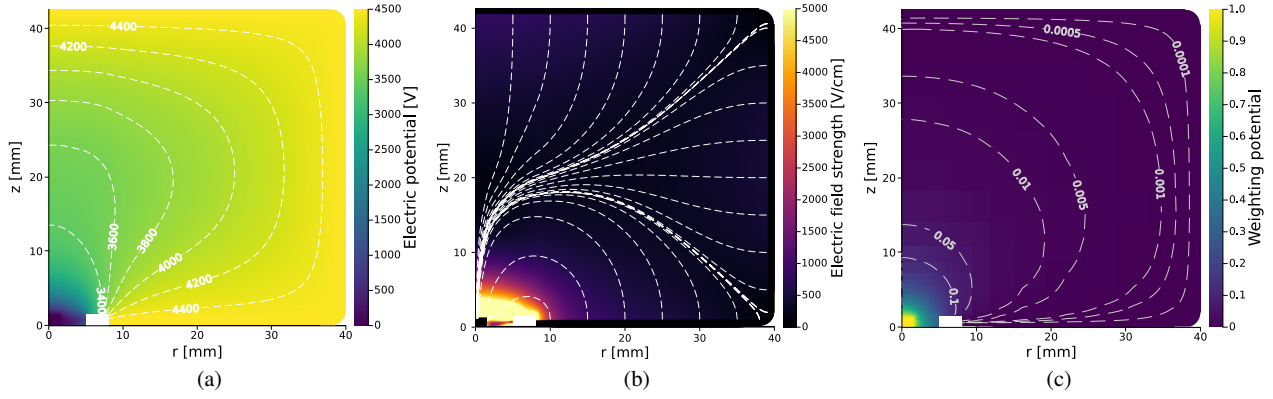
The position dependence is also evident in the pulse shapes from the RCC layer, despite the rise of the pulse shape being slowed down by the random diffusion of carriers. The fast rising edges of the pulse shapes of the RCC layer events last about 3  $\mu\text{s}$ , while those from the  $p$ - $n$  boundary last only about 10 ns. For real detector pulse shapes, which integrate the electronic response and electrical noise, the slow rise may become invisible, leaving only the fast-rising edge. During the process of triggering and signal digitization, we will also lose the information of the rise start time of the pulse shape due to the electrical noise.

#### 4.3 Non-uniformity of the RCC layer

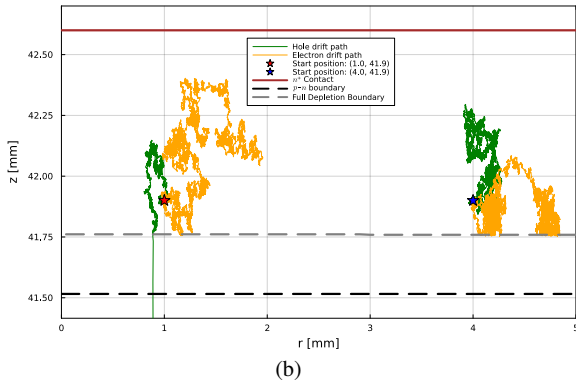
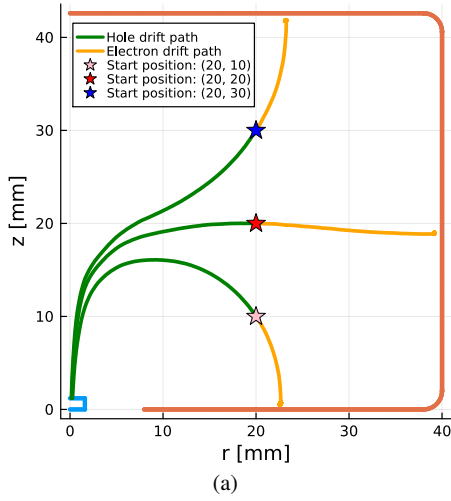
The electric field strength along the  $p$ - $n$  boundary as a function of  $\theta$ , from the groove to the top center, is presented in Figure 17. It varies within 200–800 V/cm across most positions on the side and top ( $\theta \in [-45^\circ, 90^\circ]$ ). At the bottom part of the  $p$ - $n$  boundary, the electric field strength increases steeply near the groove, reaching  $\sim 10000$  V/cm at the groove. The lowest electric field strength at the  $p$ - $n$  boundary ( $\sim 60$  V/cm) occurs at the detector corners ( $\theta$  around  $\pm 30^\circ$ ). The  $p$ - $n$  boundary electric field strength at the top center point is  $\sim 800$  V/cm.

Figure 18 presents the simulated FDD, FCCD and the depth of the  $p$ - $n$  boundary against  $\theta$ . The predicted full-depletion boundary is slightly shallower than the full CCE boundary, indicating that incomplete charge collection also occurs in the depleted region near the full-depletion boundary, due to the weak electric field and random diffusion of carriers. Figure 17 and 18 demonstrate a significant correlation between the electric field at the  $p$ - $n$  boundary and the properties of the RCC layer, namely, a stronger electric field corresponds to a larger depleted region and a larger full CCE region. At the top center ( $\theta = 90^\circ$ ), the simulated FDD and FCCD are determined to be  $(839 \pm 2) \mu\text{m}$  and  $(850 \pm 10) \mu\text{m}$ , respectively. The latter is consistent with the experimentally measured value of  $(870 \pm 67) \mu\text{m}$  [22].





**Fig. 13** The electric potential (dashed lines are the equipotential contours) (a), the electric field (white lines are the electric field lines) (b), and the weighting potential of the  $p^+$  contact (dashed lines are the equipotential contours) (c) of the BEGe detector, as calculated with *SSD.jl*.



**Fig. 14** Typical drift paths of three charge carrier pairs in the detector bulk (a) and typical drift paths of two charge carrier pairs in the RCC layer (b), simulated with *SSD.jl*. For the case in the RCC layer, within a 10  $\mu$ s time window, the hole on the left reaches the depleted region and gets collected, while the one on the right is still diffusing.

#### 4.4 CCE-corrected simulated spectrum

Figure 19a displays the simulated CCE curves for events at the top center of the detector with varying RCC layer

carrier lifetimes ( $\tau$ ), a simulated energy ( $E$ ) of 5 keV, and no self-repulsion effect. Figure 19b presents the simulated CCE curves for events at different detector positions around the top center with  $\tau = 800$  ns,  $E = 5$  keV, and no self-repulsion effect.

When the self-repulsion effect is not simulated, the carriers drift independently. Therefore, the simulated event energy affects the estimated statistical uncertainty of the CCE but not its mean value, according to Equations 22-23. However, when the effect is simulated, it can influence the charge drift, thereby affecting the mean value of CCE. Figure 19c presents the simulated CCE curves with and without the self-repulsion effect considered, while  $\tau = 800$  ns,  $r = 0$  mm, and  $E = 5$  keV. For the case with the self-repulsion effect, we also simulated the CCE curves with larger event energies in 0–200 keV, also shown in Figure 19c. The energy range was chosen to cover more than 99% of the energies deposited in the RCC layer in this case.

These results demonstrate that in this case, the  $r$ -position variation and the self-repulsion effect have a minimal impact on the CCE curve compared to the RCC layer carrier lifetimes. Therefore, to accelerate the computation, we ignored the self-repulsion effect and used the CCE curve of the top center to represent the entire top RCC layer.

By simulating energy depositions in the crystal with Geant4 and applying corrections using the simulated CCE curve, we obtained the CCE-corrected simulated energy spectrum. The simulation-related parameters are also shown in Table 1. The RCC layer carrier lifetimes were determined to be 800 ns by matching the CCE-corrected simulated spectrum with the experimental spectrum with  $\chi^2$  minimization method. As shown in Figure 20, the CCE-corrected simulated spectrum using  $\tau_{e/h,I} = 800$  ns agrees well with the experimental spectrum. About 90% of the simulated results lie within  $5\sigma$  of the experimental results (using the estimated Poisson fluctuation).

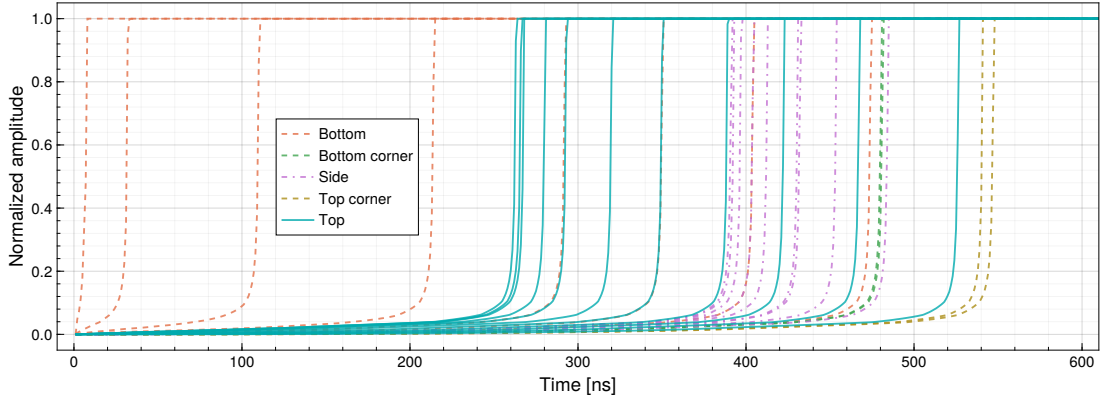


**Fig. 15** The pulse shapes of events originated at the  $p$ - $n$  boundary (in the sensitive region) at the sampling positions which are annotated in Figure 12.

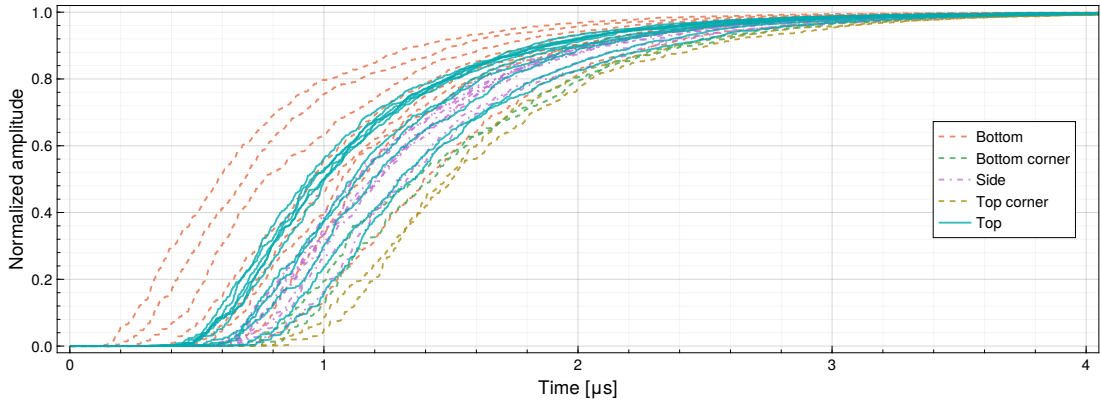


**Fig. 16** The pulse shapes of events originated at a depth of 0.5 mm from the surface (in the RCC layer) at the sampling positions which are annotated in Figure 12.

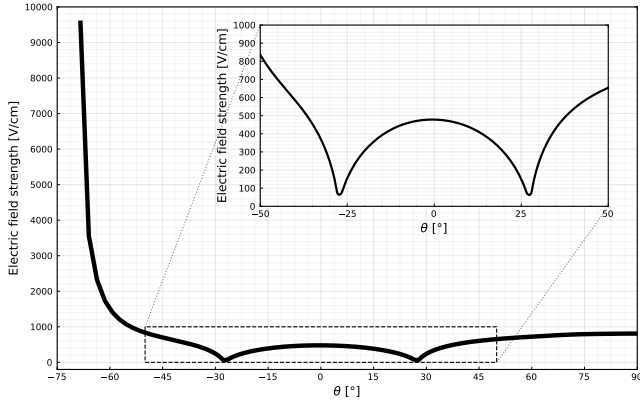


**Fig. 17** The simulated electric field strength on the  $p$ - $n$  boundary as a function of  $\theta$ .

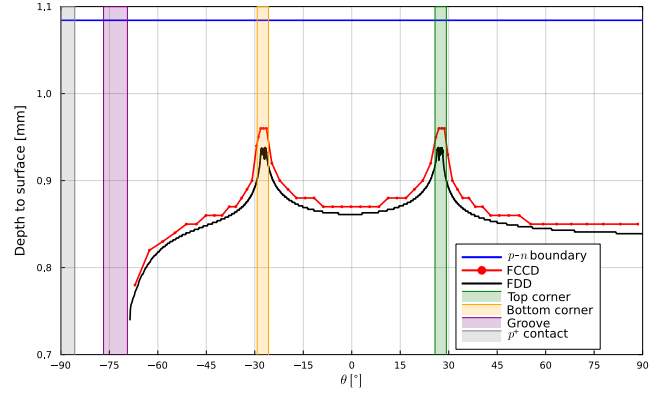


**Fig. 18** The simulated FDD (black) and FCCD (red), and the  $p$ - $n$  boundary depth (blue) as a function of  $\theta$ . Surface areas of the BEGe detector are also shown:  $p^+$  contact (gray), groove (purple), bottom corner (yellow), top corner (green), and the  $p$ - $n$  boundary (blue).

Minor discrepancies observed for some data points (mainly  $\sim 70$  keV), may arise from the oversimplification of the currently employed constant-lifetime trapping model, insufficient knowledge of the detector parameters, neglect of the position dependence of CCE, or neglect of the self-repulsion effect, listed in descending order of likelihood. The actual lifetime likely varies with depth in the RCC layer due to the

rapid change of impurity density in the RCC layer, see Figure 2. A depth-dependent-lifetime trapping model may improve simulation precision significantly and will be the subject of future work.

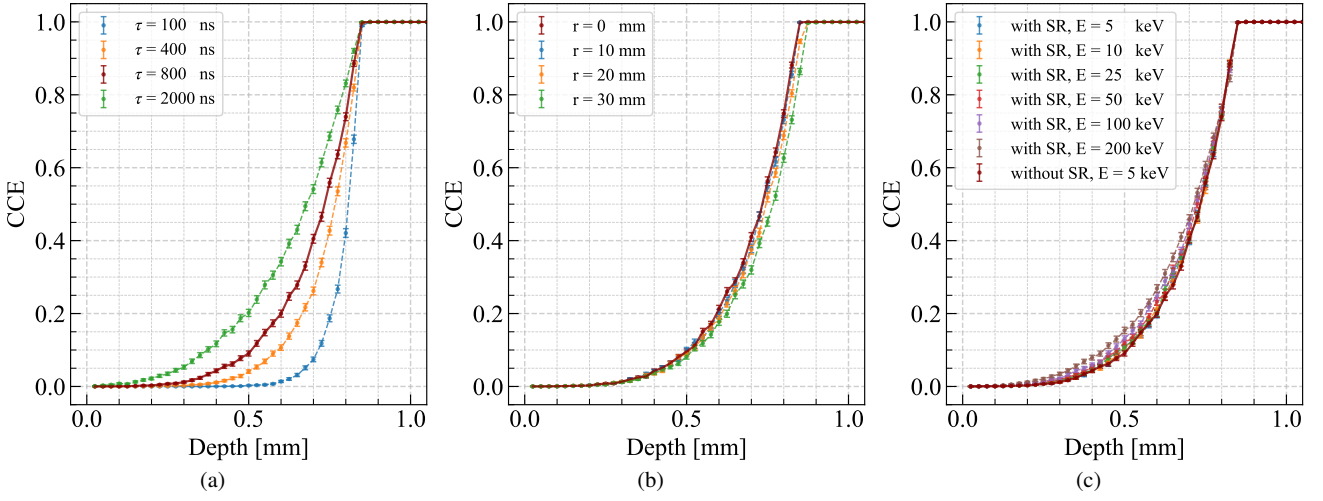


**Fig. 19** (a) CCE curves for events at the top center point of the detector ( $r = 0$  mm) with varying RCC layer carrier lifetimes ( $\tau$ ), a simulated energy ( $E$ ) of 5 keV, and no self-repulsion (SR). (b) CCE curves for events at different detector positions around the top center, with  $\tau = 800$  ns, no SR, and  $E = 5$  keV. (c) CCE curves with and without the self-repulsion, while  $\tau = 800$  ns and  $r = 0$  mm.

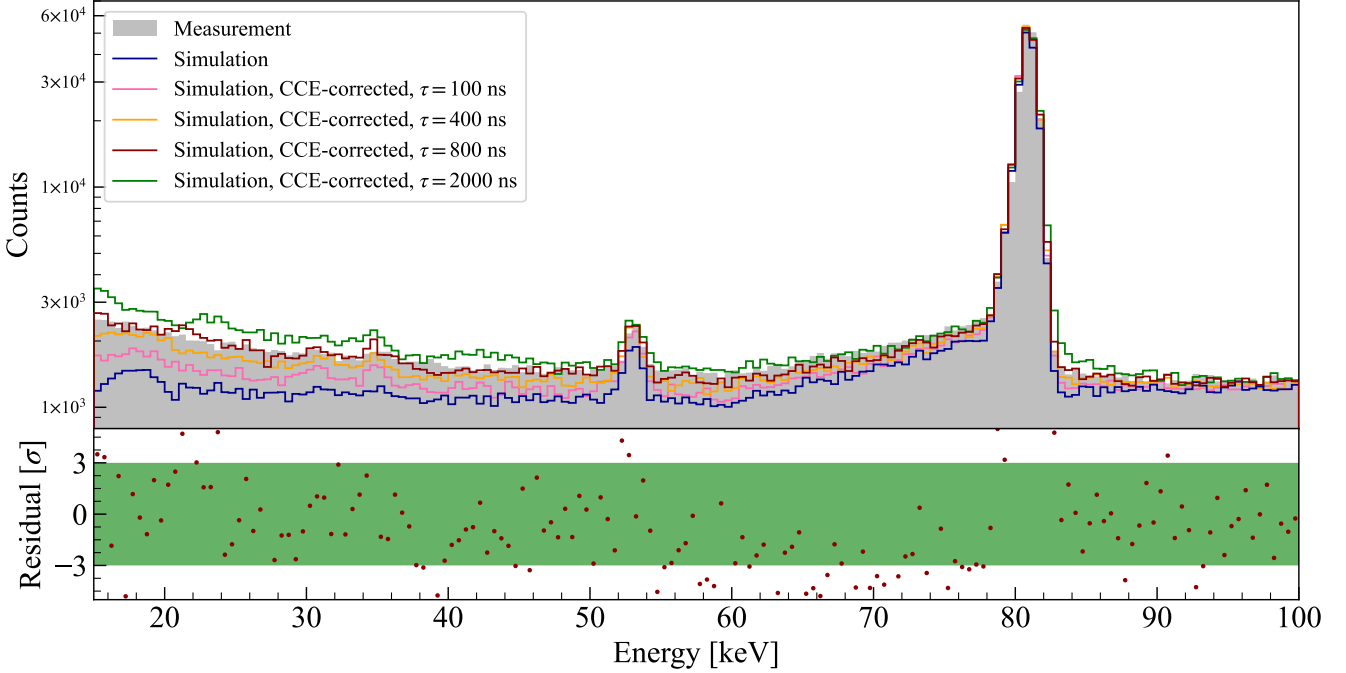


**Fig. 20** Experimentally measured energy spectrum (gray area), compared to simulated spectra that are corrected using the CCE determined with different RCC layer carrier lifetimes: 800 ns (solid red), 100 ns (dashed pink), 400 ns (dashed orange) and 2000 ns (dashed green), and simulated spectrum without CCE correction (solid blue). An RCC layer carrier lifetime of 800 ns shows the best match to the measured spectrum, determined by  $\chi^2$  minimization. The peaks around 31/35 keV and 53/81 keV originate from the X-rays (30.63/30.97/35.05/35.90 keV) and  $\gamma$ -rays (53.16/79.61/81.00 keV) of the  $^{133}\text{Ba}$  source. The bottom half of the figure shows the residuals of the simulated spectrum for this 800 ns lifetime to the measured spectrum.

## 5 Summary and outlook

We have developed and verified a novel mechanistic three-dimensional pulse shape simulation method for events originating in the reduced charge collection (RCC) surface layer of  $p$ -type HPGe detectors. This method is now publicly avail-

able as part of the open-source simulation package *SolidState-Detectors.jl*.

In our approach, we model the ionized impurity density profile of the RCC layer based on the thermal diffusion process of lithium. The hole and electron mobility models are based on a combination of ionized impurity scattering, neutral impurity scattering, and acoustic phonon scattering. We

use a random walk algorithm to simulate carrier diffusion and derive the diffusion coefficient from the mobility via the Einstein relation. Optionally, we superimpose the charge-carrier self-repulsion effect. Finally, we use a constant-lifetime trapping model to simulate carrier trapping in the RCC layer.

We have validated the simulation method against analytical calculations for a hypothetical true-coaxial HPGe detector. The time distributions for the arrival of holes at the  $p$ - $n$  boundary, the depth-dependency charge collection efficiency (CCE), and the pulse shapes all agree very well between both approaches.

We have also validated our method against a spectrum measured with an actual  $p$ -type BEGe detector. The simulated RCC layer depth at top center of the detector is consistent with the experimental measurement. We match the measured spectrum with a Monte-Carlo spectrum, with only minor discrepancies, when we simulate the charge collection using an RCC layer carrier lifetime of 800 ns. To achieve an even better agreement with the measured data, we need more accurate detector parameters, including geometry, lithium diffusion process parameters, and the acceptor impurity density profile.

So far, we have used a constant-lifetime trapping model. The actual lifetime likely varies with depth in the RCC layer due to the varying impurity density. A depth-dependent-lifetime trapping model may improve the simulation results even further and will be a subject of future work.

The novel simulation method we presented here can serve as a basis for the investigation of RCC layer physics. It also provides a new basis to develop and test novel pulse shape discrimination techniques, by generating realistic surface pulse libraries accompanied by ground truth data. This can help current and upcoming low-background experiments to use tighter background cuts with simulation-based control of systematics and cut efficiencies.

Although this paper focuses on  $p$ -type HPGe detectors, the method and code are also applicable to  $p$ -type multi-contact HPGe detectors. Moreover, with adjustments to the RCC layer impurity profile, the method and code can also be extended to  $n$ -type HPGe detectors and other types of semiconductors (e.g., Silicon, CdZnTe).

## Acknowledgments

This work was supported by the National Natural Science Foundation of China (Grant No. 12425507 and No. 12175112), the National Key Research and Development Program of China (Grant No. 2023YFA1607101 and No. 2022YFA1604701), and the PhD student fund for short-term overseas visits of Tsinghua University (Contract Number: 2024088).

## References

1. W. Zhao, Q. Yue, K. Kang et al., *Physical Review D* **88**(5), 052004 (2013). doi:[10.1103/PhysRevD.88.052004](https://doi.org/10.1103/PhysRevD.88.052004). URL <https://link.aps.org/doi/10.1103/PhysRevD.88.052004>
2. H. Jiang, L. Jia, Q. Yue et al., *Physical Review Letters* **120**(24), 241301 (2018). doi:[10.1103/PhysRevLett.120.241301](https://doi.org/10.1103/PhysRevLett.120.241301). URL <https://link.aps.org/doi/10.1103/PhysRevLett.120.241301>
3. H. Ma, Z. She, Z. Liu et al., *Journal of Physics: Conference Series* **1468**(1), 012070 (2020). doi:[10.1088/1742-6596/1468/1/012070](https://doi.org/10.1088/1742-6596/1468/1/012070). URL <https://iopscience.iop.org/article/10.1088/1742-6596/1468/1/012070>
4. H. Li, H. Liao, S. Lin et al., *Physical Review Letters* **110**(26), 261301 (2013). doi:[10.1103/PhysRevLett.110.261301](https://doi.org/10.1103/PhysRevLett.110.261301). URL <https://link.aps.org/doi/10.1103/PhysRevLett.110.261301>
5. W. Dai, H. Ma, Q. Yue et al., *Physical Review D* **106**(3), 032012 (2022). doi:[10.1103/PhysRevD.106.032012](https://doi.org/10.1103/PhysRevD.106.032012). URL <https://link.aps.org/doi/10.1103/PhysRevD.106.032012>
6. B. Zhang, J. Wang, L. Yang, *Chinese Physics C* **48**(10), 103001 (2024). doi:[10.1088/1674-1137/ad597b](https://doi.org/10.1088/1674-1137/ad597b). URL <https://iopscience.iop.org/article/10.1088/1674-1137/ad597b>
7. N. Abgrall, A. Abramov, N. Abrosimov et al., (Penang, Malaysia, 2017), p. 020027. doi:[10.1063/1.5007652](https://doi.org/10.1063/1.5007652). URL <https://pubs.aip.org/aip/acp/article/648185>
8. H. Wong, H. Li, J. Li et al., *Journal of Physics: Conference Series* **39**, 266 (2006). doi:[10.1088/1742-6596/39/1/064](https://doi.org/10.1088/1742-6596/39/1/064). URL <https://iopscience.iop.org/article/10.1088/1742-6596/39/1/064>
9. H. Bonet, A. Bonhomme, C. Buck et al., *Physical Review Letters* **126**(4), 041804 (2021). doi:[10.1103/PhysRevLett.126.041804](https://doi.org/10.1103/PhysRevLett.126.041804). URL <https://link.aps.org/doi/10.1103/PhysRevLett.126.041804>
10. L. Yang, Y. Liang, Q. Yue, in *Proceedings of XVIII International Conference on Topics in Astroparticle and Underground Physics — PoS(TAUP2023)* (Sissa Medialab, University of Vienna, 2024), p. 296. doi:[10.22323/1.441.0296](https://doi.org/10.22323/1.441.0296). URL <https://pos.sissa.it/441/296>
11. V. Belov, A. Bystryakov, M. Danilov et al., *Chinese Physics C* **49**(5), 053004 (2025). doi:[10.1088/1674-1137/adb9c8](https://doi.org/10.1088/1674-1137/adb9c8). URL <https://iopscience.iop.org/article/10.1088/1674-1137/adb9c8>

12. P. Zhang, H. Ma, L. Yang et al., *Astroparticle Physics* **158**, 102946 (2024). doi:[10.1016/j.astropartphys.2024.102946](https://doi.org/10.1016/j.astropartphys.2024.102946). URL <https://linkinghub.elsevier.com/retrieve/pii/S0927650524000239>
13. J. Herrero-Garcia, R. Patrick, A. Scaffidi, *Journal of Cosmology and Astroparticle Physics* **2022**(02), 039 (2022). doi:[10.1088/1475-7516/2022/02/039](https://doi.org/10.1088/1475-7516/2022/02/039). URL <https://iopscience.iop.org/article/10.1088/1475-7516/2022/02/039>
14. M. Agostini, G. Araujo, A.M. Bakalyarov et al., *The European Physical Journal C* **82**(4), 284 (2022). doi:[10.1140/epjc/s10052-022-10163-w](https://doi.org/10.1140/epjc/s10052-022-10163-w). URL <https://link.springer.com/10.1140/epjc/s10052-022-10163-w>
15. P. Holl, L. Hauertmann, B. Majorovits et al., *The European Physical Journal C* **79**(6), 450 (2019). doi:[10.1140/epjc/s10052-019-6869-2](https://doi.org/10.1140/epjc/s10052-019-6869-2). URL <http://link.springer.com/10.1140/epjc/s10052-019-6869-2>
16. S. Delaquis, M. Jewell, I. Ostrovskiy et al., *Journal of Instrumentation* **13**(08), P08023 (2018). doi:[10.1088/1748-0221/13/08/p08023](https://doi.org/10.1088/1748-0221/13/08/p08023). URL <https://iopscience.iop.org/article/10.1088/1748-0221/13/08/p08023>
17. A. Radovic, M. Williams, D. Rousseau et al., *Nature* **560**(7716), 41 (2018). doi:[10.1038/s41586-018-0361-2](https://doi.org/10.1038/s41586-018-0361-2). URL <http://www.nature.com/articles/s41586-018-0361-2>
18. T. Cohen, M. Freytsis, B. Ostdiek, *Journal of High Energy Physics* **2018**(2), 34 (2018). doi:[10.1007/JHEP02\(2018\)034](https://doi.org/10.1007/JHEP02(2018)034). URL [http://link.springer.com/10.1007/JHEP02\(2018\)034](http://link.springer.com/10.1007/JHEP02(2018)034)
19. I. Abt, F. Fischer, F. Hagemann et al., *Journal of Instrumentation* **16**(08), P08007 (2021). doi:[10.1088/1748-0221/16/08/p08007](https://doi.org/10.1088/1748-0221/16/08/p08007). URL <https://iopscience.iop.org/article/10.1088/1748-0221/16/08/p08007>
20. F. Hagemann, Determination of the impurity density profile and charge carrier mobilities in a point-contact germanium detector using a novel Compton Scanner. Ph.D. thesis, Technische Universität München (2024)
21. I. Abt, C. Gooch, F. Hagemann et al., *The European Physical Journal C* **83**(5), 352 (2023). doi:[10.1140/epjc/s10052-023-11509-8](https://doi.org/10.1140/epjc/s10052-023-11509-8). URL <https://link.springer.com/10.1140/epjc/s10052-023-11509-8>
22. W. Dai, H. Ma, Q. Yue et al., *Applied Radiation and Isotopes* **193**, 110638 (2023). doi:[10.1016/j.apradiso.2022.110638](https://doi.org/10.1016/j.apradiso.2022.110638). URL <https://linkinghub.elsevier.com/retrieve/pii/S0969804322005231>
23. H. Li, L. Singh, M.K. Singh et al., *Astroparticle Physics* **56**, 1 (2014). doi:[10.1016/j.astropartphys.2014.02.005](https://doi.org/10.1016/j.astropartphys.2014.02.005). URL <https://linkinghub.elsevier.com/retrieve/pii/S0927650514000176>
24. L. Yang, H. Li, H. Wong et al., *Nuclear Instruments and Methods in Physics Research Section A: Accelerators, Spectrometers, Detectors and Associated Equipment* **886**, 13 (2018). doi:[10.1016/j.nima.2017.12.078](https://doi.org/10.1016/j.nima.2017.12.078). URL <https://linkinghub.elsevier.com/retrieve/pii/S0168900217314961>
25. R. Li, S. Liu, S. Lin et al., *Nuclear Science and Techniques* **33**(5), 57 (2022). doi:[10.1007/s41365-022-01041-x](https://doi.org/10.1007/s41365-022-01041-x). URL <https://link.springer.com/10.1007/s41365-022-01041-x>
26. J. Wang, M.K. Singh, H. Li et al., *The European Physical Journal C* **85**(3), 331 (2025). doi:[10.1140/epjc/s10052-025-14051-x](https://doi.org/10.1140/epjc/s10052-025-14051-x). URL <https://link.springer.com/10.1140/epjc/s10052-025-14051-x>
27. K. Huang, *Semiconductor physics* (Science Press, Beijing, 2012)
28. G.F. Knoll, *Radiation detection and measurement*, 4th edn. (John Wiley, Hoboken, N.J, 2010)
29. W. Dai, Pulse shape analysis of cdex high purity germanium detector and direct detection of exotic dark matter. Ph.D. thesis, Tsinghua University (2024)
30. H. Mei, D. Mei, G. Wang et al., *Journal of Instrumentation* **11**(12), P12021 (2016). doi:[10.1088/1748-0221/11/12/P12021](https://doi.org/10.1088/1748-0221/11/12/P12021). URL <https://iopscience.iop.org/article/10.1088/1748-0221/11/12/P12021>
31. H. Mei, G. Wang, G. Yang et al., *Journal of Instrumentation* **12**(07), P07003 (2017). doi:[10.1088/1748-0221/12/07/P07003](https://doi.org/10.1088/1748-0221/12/07/P07003). URL <https://iopscience.iop.org/article/10.1088/1748-0221/12/07/P07003>
32. E.E. Haller, W.L. Hansen, F.S. Goulding, *Advances in Physics* **30**(1), 93 (1981). doi:[10.1080/00018738100101357](https://doi.org/10.1080/00018738100101357). URL <https://doi.org/10.1080/00018738100101357>
33. E.E. Haller, W.L. Hansen, P. Luke et al., *IEEE Transactions on Nuclear Science* **29**(1), 745 (1982). doi:[10.1109/TNS.1982.4335949](https://doi.org/10.1109/TNS.1982.4335949). URL <https://ieeexplore.ieee.org/document/4335949/>
34. S.E. Boggs, S.N. Pike, J. Roberts et al., *Nuclear Instruments and Methods in Physics Research Section A: Accelerators, Spectrometers, Detectors and Associated Equipment* **1057**, 168756 (2023). doi:[10.1016/j.nima.2023.168756](https://doi.org/10.1016/j.nima.2023.168756). URL <https://www.sciencedirect.com/science/article/pii/S0168900223007477>
35. Z. He, *Nuclear Instruments and Methods in Physics Research Section A: Accelerators, Spectrometers, Detectors and Associated Equipment* **463**(1-2), 250 (2001). doi:[10.1016/S0168-9002\(01\)00223-6](https://doi.org/10.1016/S0168-9002(01)00223-6). URL <https://linkinghub.elsevier.com/retrieve/pii/S0168900201002236>
36. J. Ma, Q. Yue, Q. Wang et al., *Applied Radiation and Isotopes* **127**, 130 (2017).



- doi:[10.1016/j.apradiso.2017.05.023](https://doi.org/10.1016/j.apradiso.2017.05.023). URL <https://linkinghub.elsevier.com/retrieve/pii/S096980431630817X>
37. B. Zhang, Searching for  $^{76}\text{Ge}$  neutrinoless double beta decay with CDEX-1B experiment. Master's thesis, Tsinghua University (2023)
38. H. Jiang, Q. Yue, Y. Li et al., Chinese Physics C **40**(9), 096001 (2016). doi:[10.1088/1674-1137/40/9/096001](https://doi.org/10.1088/1674-1137/40/9/096001). URL <https://iopscience.iop.org/article/10.1088/1674-1137/40/9/096001>
39. S. Agostinelli, J. Allison, K. Amako et al., Nuclear Instruments and Methods in Physics Research Section A: Accelerators, Spectrometers, Detectors and Associated Equipment **506**(3), 250 (2003). doi:[10.1016/S0168-9002\(03\)01368-8](https://doi.org/10.1016/S0168-9002(03)01368-8). URL <https://linkinghub.elsevier.com/retrieve/pii/S0168900203013688>
40. J. Allison, K. Amako, J. Apostolakis et al., IEEE Transactions on Nuclear Science **53**(1), 270 (2006). doi:[10.1109/TNS.2006.869826](https://doi.org/10.1109/TNS.2006.869826). URL <http://ieeexplore.ieee.org/document/1610988/>
41. J. Allison, K. Amako, J. Apostolakis et al., Nuclear Instruments and Methods in Physics Research Section A: Accelerators, Spectrometers, Detectors and Associated Equipment **835**, 186 (2016). doi:[10.1016/j.nima.2016.06.125](https://doi.org/10.1016/j.nima.2016.06.125). URL <https://www.sciencedirect.com/science/article/pii/S0168900216306957>